Numerical simulation of temperature-driven free surface flows, with application to laser melting and polishing

Alexandre Caboussat [a,*], Julien Hess [b,c], Alexandre Masserey [b,d], Marco Picasso [c]

[a] *Geneva School of Business Administration, University of Applied Sciences and Arts Western Switzerland (HES-SO), 1227 Carouge, Switzerland*
[b] *Ycoor Systems SA, 3960 Sierre, Switzerland*
[c] *Institute of Mathematics, Ecole polytechnique fédérale de Lausanne, 1015 Lausanne, Switzerland*
[d] *Thermomechanical Metallurgy Laboratory, Ecole polytechnique fédérale de Lausanne, 1015 Lausanne, Switzerland*

ARTICLE INFO

ABSTRACT

We present a multi-physics model for the approximation of the coupled system formed by the heat equation and the Navier-Stokes equations with solidification and free surfaces. The computational domain is the union of two overlapping regions: a larger domain to account for thermal effects, and a smaller region to account for the fluid flow. Temperature-dependent surface effects are accounted for via surface tension and Marangoni forces. The volume-of-fluid approach is used to track the free surfaces between the metal (liquid or solidified) and the ambient air. The numerical method incorporates all the physical phenomena within an operator splitting strategy. The discretization relies on a two-grid approach that uses an unstructured finite element mesh for diffusion phenomena and a structured Cartesian grid for advection phenomena. The model is validated through numerical experiments, the main application being laser melting and polishing.

1. Introduction

The coupling between incompressible flow equations and thermal effects for the solidification of a metal alloy is important in mold casting, when regulating the solidification in order to ensure quality requirements [1–3], or when re-melting a metal in laser polishing processes [4–10]. Other examples include solidification of droplets [11], vaporization [12], or powder sintering in additive manufacturing and 3D printing [13–16]. For all these applications, a model for an incompressible liquid flow with a free surface is coupled to heat transfer, and the behavior of the free surface is strongly temperature-dependent. The complexity of the problem does not only come from the thermal and fluid equations, but from the very nonlinear coupling through the evolution of sharp free surfaces, between the metal and the ambient air, as well as the evolution of melting fronts [17,18].

The main application of interest in this article is the shallow laser surface melting (SLSM) process. A heat source created by a laser source induces a melting at the surface of a thin piece of metal. The melting zone remains shallow, and, when solidifying again, the surface of the metal is polished due to the redistribution of the liquid material over the surface. The evolution of the surface tension with temperature is a crucial factor for such a process. Several numerical methods exist in the literature for such an application, see, e.g., [12,19–22]. We are focusing in this work on polishing processes, for which it is particularly important not to provoke material loss. For such processes, the temperature remains below the evaporation temperature and therefore evaporation can be neglected. This "melting only" regime is documented, e.g., in [23].

---

* Corresponding author.
E-mail address: alexandre.caboussat@hesge.ch (A. Caboussat).
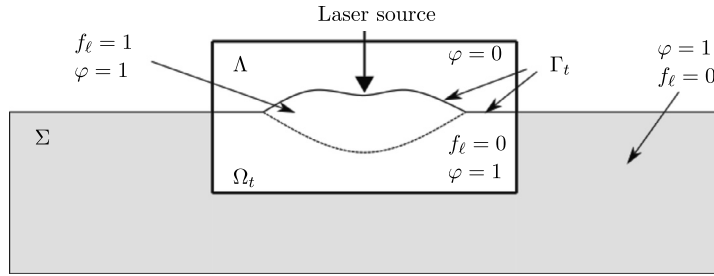
Fig. 1. Laser melting of a thin metal plate. 2D sketch of the geometrical domain. The cavity Λ is highlighted in bold, while Σ is the gray region. At each time $t \in (0, t_{max})$, the metal domain $\Omega_t \cup \Sigma \subset \Lambda \cup \Sigma$ is separated from the ambient air by the metal-air interface Γ_t in Λ.

The main characteristic of the method presented here is that it allows to couple solidification process and tracking of free surfaces, with a well-proven algorithmic approach. It decouples the transport and diffusion operators in the thermal and fluid flow equations. Moreover, two different domains are considered for the thermal and fluid flow effects, and the method uses two different grids to solve the transport and diffusion equations.

A mathematical model for the numerical simulation of Newtonian fluids with free surfaces, without temperature effects, has been presented and validated in [24–27]. It has successfully been extended to viscoelastic flow [28] and to the retreat of Alpine glaciers [29]. It is extended here to include temperature and solidification effects, together with Marangoni effects on the free surfaces.

We consider a domain representing an incompressible metal (liquid or solidified), with free surfaces in contact with the ambient air. The incompressible Navier-Stokes equations with solidification are coupled with an enthalpy-based convection-diffusion heat equation for heat transfer effects. The solidification process is taken into account using a Boussinesq approximation, and a coupling with the Darcy equation thanks to a Carman-Kozeny approximation term [30]. Since the temperature-driven effects induce the creation of melting and solidification of the liquid phase, a penalization model is chosen to be able to describe liquid, solid and mushy zones [30]. The surface effects on the free surface between liquid metal and air include temperature-dependent physical parameters. The varying surface tension coefficient leads to the creation of motion in the liquid metal called *Marangoni effects* [31–33]. The system of equations is supplemented with appropriate boundary and initial conditions. The novelty of the proposed approach lies in the choice of a dedicated numerical method proposed to solve this multiphysics model, which couples flow equations, heat transfer, solidification and free surfaces, with a multidomain approach for the computational domain.

An operator splitting approach is advocated to decouple the diffusion operators (heat diffusion and the Stokes model) and the advection operators (transport of quantities), and capture the complex interactions between the fluid dynamics and the thermal effects [34]. Adequate numerical algorithms for the simulation of thermal effects (fusion, solidification, etc.) into the fluid flow solver are proposed. The volume fraction of liquid approach is used to track the free surfaces between the (liquid or solidified) metal and the ambient air [35].

The space discretization relies on a two-grids method that uses an unstructured finite element mesh for the diffusion phenomena, and a structured Cartesian grid for the advection phenomena (convection of temperature, velocity and volume fraction) [36]. A multi-domain approach is advocated in order to solve the multi-physics problem; in particular, the flow equations are considered in a smaller subset of the computational domain. A local mesh cutting technique is incorporated in order to accurately track the free surfaces, as well as provide an accurate description of the surface effects and forces (see, e.g., [26]).

Benchmarking experiments are used to validate the convergence properties of the proposed method [37]. In particular, the sensitivity of the influence of Marangoni effects on a liquid metal is investigated. Finally, we highlight results for the application to the re-melting, solidification and polishing in laser processes.

The article is structured as follows. In Section 2, we describe the mathematical model, while Sections 3 and 4 detail respectively the time and space discretizations. The results of numerical experiments are presented in Section 5, to validate the numerical methods, to benchmark on classical test cases, and to finally address the process of laser melting.

2. Mathematical model

Let us consider Λ and Σ two bounded non-overlapping domains in $\mathbb{R}^3$ arranged as illustrated in Fig. 1, and let $t_{max} > 0$ be the final time of the simulation. The domain Σ contains solidified metal only. For any given time $t \in (0, t_{max})$, let $\Omega_t \subset \Lambda$ be the domain occupied by the metal (solidified or not) and $\Gamma_t := \partial \Omega_t \backslash \partial \Lambda$ be the free surface between the metal and the ambient air that is embedded in Λ, namely the boundary of the metal domain that is not in contact with the boundary of the cavity Λ. Thus the full domain occupied by the metal is $\Omega_t \cup \Sigma$.

The rationale behind this setup is to consider a multi-domain approach in order solve a heat equation in $\Omega_t \cup \Sigma$, and the fluid dynamics with free surfaces in Ω_t only, as both problems occur on different scales. Fig. 1 typically illustrates a 2D setup for the laser polishing of a metal plate.

The mathematical model reads as follows. Let Q denote the restricted space-time domain containing the metal that is included in $\Lambda \times (0, t_{max})$:

$$Q = \{(\mathbf{x}, t) : 0 < t < t_{max}, \ \mathbf{x} \in \Omega_t\},$$

and let R denote the full space-time domain containing the metal, that is

$$R = \{(\mathbf{x}, t) : 0 < t < t_{max}, \ \mathbf{x} \in \Omega_t \cup \Sigma\}.$$

Assuming that Q is sufficiently regular, the velocity field $\mathbf{v} : Q \to \mathbb{R}^3$ and the pressure field $p : Q \to \mathbb{R}$ are assumed to satisfy incompressible, time-dependent Navier-Stokes equations, with an additional Darcy-like reaction term modeling the solidification process. The corresponding set of equations reads:

$$\rho \frac{\partial \mathbf{v}}{\partial t} + \rho(\mathbf{v} \cdot \nabla)\mathbf{v} - 2\nabla \cdot (\mu \mathbf{D}(\mathbf{v})) + \alpha(T)\mathbf{v} + \nabla p = \mathbf{f}(T), \tag{2.1}$$

$$\nabla \cdot \mathbf{v} = 0. \tag{2.2}$$

Here $\mathbf{D}(\mathbf{v}) = \frac{1}{2}(\nabla \mathbf{v} + \nabla \mathbf{v}^T)$ is the symmetric deformation tensor, ρ and μ are respectively the density and the viscosity of the metal and $\mathbf{f}$ denotes the external forces, which typically incorporate gravity effects $\rho \mathbf{g}$ (with $\mathbf{g}$ the gravity acceleration). Note that the external forces may be temperature-dependent and contribute to the coupling between all equations. The term $\alpha(T)$ depends on the temperature, and is defined below.

In order to model solidification with a diffuse model (mushy zone), the velocity is penalized with an additional Carman-Kozeny term, which represents the coupling with Darcy flow in porous media [30]. The reaction coefficient in (2.1) is thus given by:

$$\alpha(T) = \bar{\alpha} \frac{\mu(1 - f_\ell(T))^2}{(f_\ell(T) + \varepsilon)^3}, \tag{2.3}$$

where $f_\ell = f_\ell(T)$ is the liquid fraction, which equals one in the liquid region (above the temperature of fusion) and zero in the solid region, and $\bar{\alpha}$ is a constant to be calibrated. Note that $0 < \varepsilon << 1$ is a numerical parameter to avoid a division by zero.

The temperature field $T : R \to \mathbb{R}$ and the enthalpy $\mathcal{H} : R \to \mathbb{R}$ are assumed to satisfy the classical enthalpy formulation of the heat conservation equation in the full space-time domain, which can be derived by general energy conservation equation simplified with Fourier's law (see [30] for details). The corresponding set of equations reads:

$$\frac{\partial \mathcal{H}}{\partial t} + \mathbf{v} \cdot \nabla \mathcal{H} - \nabla \cdot (k(T)\nabla T) = S. \tag{2.4}$$

Here $k(T)$ is the thermal conductivity of the metal, and S is a potential heat source. The relationship between enthalpy and temperature is given by $T := \beta(\mathcal{H})$, and reciprocally

$$\mathcal{H}(T) = \int_0^T \rho C_p(s)ds + L \cdot f_\ell(T) \tag{2.5}$$

where C_p is the specific heat and L is the latent heat.

Remark 1. The penalization of the velocity in (2.1)–(2.2) is achieved through the reaction term $\alpha(T)$, whereas the viscosity is assumed to be constant. As observed for instance in [38,39], a penalization via the reaction term is suitable for small values of the liquid fraction f_ℓ, while a penalization via the viscosity is more suitable for modeling rigid motions. Numerical experiments reported in Section 5 have a very small mushy zone, thus justifying the use of a constant viscosity.

Remark 2. The evaporation phenomenon is not incorporated in the model. However, a potential extension based on the approach in [40] would allow to incorporate evaporation via a modification of the enthalpy-temperature diagram.

Let $\varphi : \Lambda \times (0, t_{max}) \to \{0, 1\}$ be the volume fraction of metal, which equals one if metal is present and zero otherwise. Since metal is present in Σ by definition, the volume fraction φ is defined only in Λ. The function φ is thus the characteristic function of the metal domain:

$$\Omega_t = \{\mathbf{x} \in \Lambda : \varphi(\mathbf{x}, t) = 1\}.$$

In order to describe the kinematics of the free surface, the characteristic function φ must satisfy (in a weak sense):

$$\frac{\partial \varphi}{\partial t} + \mathbf{v} \cdot \nabla \varphi = 0 \qquad \text{in } \Lambda \times (0, t_{max}), \tag{2.6}$$

where $\mathbf{v}$ in $\{\Lambda \times (0, t_{max})\} \backslash Q$ is a regular extension of $\mathbf{v}$ inside Q (see, e.g., [36]). The volume fraction of metal $\varphi(\cdot, 0)$ is given at initial time in Λ, which is equivalent to defining the initial metal region $\Omega_0 = \{\mathbf{x} \in \Lambda : \varphi(\mathbf{x}, 0) = 1\}$. The initial velocity field is also prescribed in Ω_0, while the initial enthalpy and temperature fields are prescribed in $\Omega_0 \cup \Sigma$. Boundary conditions are associated to (2.6) on the inlet part of $\partial \Lambda$ (if any), and the volume fraction is set to one on the inlet part of $\partial \Lambda$ (if any).

The Navier-Stokes equations (2.1)–(2.2) are completed with slip or no-slip boundary conditions imposed on the boundary of the metal domain $\partial \Omega_t$ that is in contact with the boundary of the cavity $\partial \Lambda$.

Surface tension and Marangoni effects on the liquid metal-air interface are taken into account via a force term on the free surface Γ_t [31,41]. The ambient air or gas is assumed to have little influence on the metal, and is treated as vacuum. The boundary condition on the metal-air interface $\Gamma_t = \partial \Omega_t \backslash \partial \Lambda$ is thus given by:

$$-p\mathbf{I} + 2\mu \mathbf{D}(\mathbf{v}) = \gamma \kappa \mathbf{n}_{\Gamma_t} + \nabla_{\Gamma_t} \gamma, \qquad \text{on} \quad \Gamma_t, \tag{2.7}$$

where $\mathbf{n}_{\Gamma_t}$ is the external unit normal vector to Γ_t towards the vacuum, κ is the curvature of Γ_t, and γ is the surface tension coefficient. In the sequel, we assume that $\gamma = \gamma(T)$ only depends on the temperature, so that the surface gradient term $\nabla_{\Gamma_t} \gamma$ may be written as

$$\nabla_{\Gamma_t} \gamma = \gamma'(T) \nabla T \cdot \mathbf{t}_1 + \gamma'(T) \nabla T \cdot \mathbf{t}_2,$$

where $\mathbf{t}_i$, $i = 1, 2$, are two linearly independent vectors in the tangent plane to Γ_t that is perpendicular to $\mathbf{n}_{\Gamma_t}$.

The boundary conditions for the heat equation (2.4) are as follows: the laser source is modeled via a prescribed heat flux on the boundary Γ_t of the metal domain, while adiabatic boundary conditions are typically applied on the rest of the boundary, namely $\partial(\Omega_t \cup \Sigma) \backslash \Gamma_t$. More precisely, the laser source condition is written as

$$k \frac{\partial T}{\partial \mathbf{n}_{\Gamma_t}} = g_f \quad \text{on} \; \Gamma_t,$$

where g_f is a given heat flux.

To summarize, the coupled multiphysics problem consists in finding the time evolution of the position of the volume fraction of metal φ in $\Lambda \times (0, t_{max})$, together with the temperature T and the enthalpy $\mathcal{H}$ in R, and the velocity $\mathbf{v}$ and the pressure p in Q only.

3. Time discretization

The implicit splitting algorithm of order one described in [25,27,36] for Newtonian flows is extended here to temperature-dependent free surface flows in multiple domains. It relies on *operator splitting* and on a *two-grid* method: the splitting algorithm decouples advection and diffusion phenomena, while the two-grid method allows to increase the accuracy of the approximation of the free surface by considering a finer grid for the approximation of advection problems.

Let $0 = t^0 < t^1 < t^2 < \ldots < t^N = t_{max}$ be a subdivision of the time interval $[0, t_{max}]$ and $\tau^n := t^{n+1} - t^n$ be the $(n+1)$th time step, $n = 0, 1, 2, \ldots, N - 1$. The operator splitting algorithm is described as follows, and illustrated in Fig. 2.

Assume that $\varphi^n : \Lambda \to \mathbb{R}$ is an approximation of φ at time t^n, which defines the metal domain $\Omega^n \cup \Sigma = \{\mathbf{x} \in \Lambda : \varphi^n(\mathbf{x}) = 1\} \cup \Sigma$. Let $\mathbf{v}^n, p^n$ be known approximations of $\mathbf{v}, p$ in Ω^n at time t^n, and let $T^n, \mathcal{H}^n$ be known approximations of $T, \mathcal{H}$ in $\Omega^n \cup \Sigma$ at time t^n. Then the approximations $\varphi^{n+1}, \Omega^{n+1}, \mathbf{v}^{n+1}, p^{n+1}, T^{n+1}, \mathcal{H}^{n+1}$ at time t^{n+1} are computed by means of a splitting algorithm as illustrated in Fig. 2. First, the diffusion-only heat equation (without convection term) allows to determine predictions of the enthalpy $\mathcal{H}^{n+1/2}$ and temperature $T^{n+1/2}$ in $\Omega^n \cup \Sigma$. Then, a generalized Stokes problem, which incorporates the temperature-dependent Carman-Kozeny term and free surface forces, is solved in order to obtain the predicted velocity $\mathbf{v}^{n+1/2}$ and the pressure p^{n+1} in Ω^n. Finally, three advection problems are solved in order to obtain the new volume fraction of metal φ^{n+1} (and thus the new metal domain Ω^{n+1}), the corrected velocity $\mathbf{v}^{n+1}$ and the corrected enthalpy $\mathcal{H}^{n+1}$ and the corrected temperature T^{n+1} in Ω^{n+1}.

3.1. Thermal step

The domain Ω^n being given, we consider the computational metal domain $\Omega^n \cup \Sigma$. The advection operator of (2.4) being handled in the advection step below, an implicit scheme is considered in order to obtain a prediction of the enthalpy and temperature. More precisely, we solve: find $\mathcal{H} : \Omega^n \cup \Sigma \to \mathbb{R}$ satisfying

$$\frac{\partial \mathcal{H}}{\partial t} - \nabla \cdot (k(T) \nabla T) = S \qquad \text{in } \Omega^n \cup \Sigma, \tag{3.1}$$
$$T = \beta(\mathcal{H}), \tag{3.2}$$

with initial conditions provided by $\mathcal{H}^n$ and given boundary conditions. We use the so called Chernoff numerical scheme [42–46], which consists in computing a pseudo-temperature $\tilde{T}^{n+1/2}$ such that:
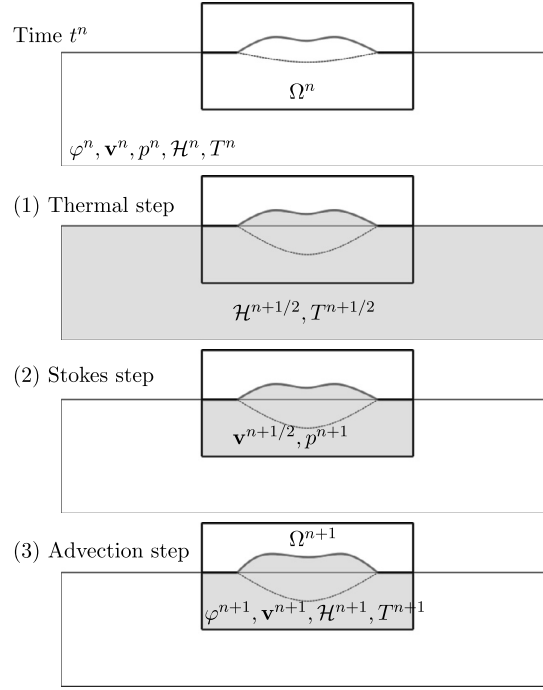
Fig. 2. Operator splitting algorithm (from top to bottom). At each time step n, we first solve the thermal equation (without convection) to determine the predicted enthalpy $H^{n+1/2}$ and temperature $T^{n+1/2}$. Then, a generalized Stokes problem is solved in order to obtain the predicted velocity $\mathbf{v}^{n+1/2}$ and the pressure p^{n+1}. Finally, three advection problems are solved in order to obtain the new volume fraction of metal φ^{n+1} (and thus the new metal domain Ω^{n+1}), the corrected velocity $\mathbf{v}^{n+1}$ and the corrected enthalpy $\mathcal{H}^{n+1}$ and corrected temperature T^{n+1}. The shaded regions describe the computational domain for each step.

$$\frac{\tilde{T}^{n+1/2} - \beta(\mathcal{H}^n)}{\tau^n} - \nabla \cdot \left(k(T^n)\nabla \tilde{T}^{n+1/2} \right) = S^{n+1}, \tag{3.3}$$

and then the enthalpy:

$$\mathcal{H}^{n+1/2} = \mathcal{H}^n + \xi(\tilde{T}^{n+1/2} - \beta(\mathcal{H}^n)), \tag{3.4}$$

where ξ is a positive relaxation parameter (sufficiently small to guarantee stability [42]) with $\xi \neq 1/\beta'(H)$. Finally, we compute the temperature $T^{n+1/2}$ as

$$T^{n+1/2} = \beta(\mathcal{H}^{n+1/2}). \tag{3.5}$$

Once the temperature $T^{n+1/2}$ is known, one can calculate the liquid fraction and update the reaction term for the Stokes problem as $\alpha^{n+1/2} = \alpha(T^{n+1/2})$, which penalizes the velocity where the metal is solidified.

3.2. Stokes step

Then, a generalized Stokes problem is solved in order to obtain the predicted velocity $\mathbf{v}^{n+1/2}$ and the pressure p^{n+1} in the restricted metal domain Ω^n, by solving (together with the natural force condition on the metal-air interface, as described below):

$$\rho \frac{\partial \mathbf{v}}{\partial t} - 2\nabla \cdot (\mu \mathbf{D}(\mathbf{v})) + \alpha(T^{n+1/2})\mathbf{v} + \nabla p = \mathbf{f}(T^{n+1/2}), \tag{3.6}$$

$$\nabla \cdot \mathbf{v} = 0. \tag{3.7}$$

An implicit Euler scheme is used for the time discretization of this Stokes system in Ω^n:

$$\rho \frac{\mathbf{v}^{n+1/2} - \mathbf{v}^n}{\tau^n} - 2\nabla \cdot \left(\mu \mathbf{D}(\mathbf{v}^{n+1/2}) \right) + \nabla p^{n+1}$$
$$+ \alpha(T^{n+1/2})\mathbf{v}^{n+1/2} = \mathbf{f}(T^{n+1/2}), \tag{3.8}$$

$$\nabla \cdot \mathbf{v}^{n+1/2} = 0, \tag{3.9}$$

with no-slip or pure-slip conditions on the boundary of the cavity $\partial \Lambda$ and the natural force condition on the metal-air interface:

$$-p^{n+1}\mathbf{I} + 2\mu \mathbf{D}(\mathbf{v}^{n+1/2}) = \gamma(T^{n+1/2})\kappa^n \mathbf{n}_{\Gamma^n} + \nabla_{\Gamma^n}\gamma(T^{n+1/2}), \quad \text{on } \Gamma^n = \partial \Omega^n \backslash \partial \Lambda,$$

where κ^n is the curvature of Γ^n. Surface tension effects are taken into account according to [47].

3.3. Advection step

Finally, considering the advection operators in (2.1), (2.4) and (2.6), the last step consists in using the velocity approximation $\mathbf{v}^{n+1/2}$ in order to transport the volume fraction of metal φ^n, the enthalpy $\mathcal{H}^{n+1/2}$ and the velocity $\mathbf{v}^{n+1/2}$ itself. It allows to obtain the new volume fraction of metal φ^{n+1} (and thus the new metal domain Ω^{n+1}), the corrected velocity $\mathbf{v}^{n+1}$ and the corrected enthalpy $\mathcal{H}^{n+1}$.

More precisely, this advection step consists in solving, between t^n and t^{n+1} the following system of nonlinear equations:

$$\frac{\partial \varphi}{\partial t} + \mathbf{v} \cdot \nabla \varphi = 0, \tag{3.10}$$

$$\frac{\partial \mathcal{H}}{\partial t} + \mathbf{v} \cdot \nabla \mathcal{H} = 0, \tag{3.11}$$

$$\frac{\partial \mathbf{v}}{\partial t} + (\mathbf{v} \cdot \nabla)\mathbf{v} = 0, \tag{3.12}$$

with initial conditions φ^n, $\mathcal{H}^{n+1/2}$ and $\mathbf{v}^{n+1/2}$ respectively.

Since the characteristics are straight lines between t^n et t^{n+1}, this system of hyperbolic equations can be solved exactly with a forward characteristics method, so that φ^{n+1}, H^{n+1} and $\mathbf{v}^{n+1}$ are respectively given by

$$\varphi^{n+1}(\mathbf{x} + \tau^n \mathbf{v}^{n+1/2}(\mathbf{x})) = \varphi^n(\mathbf{x}), \tag{3.13}$$

$$\mathcal{H}^{n+1}(\mathbf{x} + \tau^n \mathbf{v}^{n+1/2}(\mathbf{x})) = \mathcal{H}^{n+1/2}(\mathbf{x}), \tag{3.14}$$

$$\mathbf{v}^{n+1}(\mathbf{x} + \tau^n \mathbf{v}^{n+1/2}(\mathbf{x})) = \mathbf{v}^{n+1/2}(\mathbf{x}), \tag{3.15}$$

for all $\mathbf{x} \in \Omega^n$. The new domain Ω^{n+1} is then defined as $\Omega^{n+1} = \{\mathbf{x} \in \Lambda : \varphi^{n+1}(\mathbf{x}) = 1\}$, and the new metal domain is defined as $\Omega^{n+1} \cup \Sigma$.

4. Space discretization

4.1. Two-grids method

In order to solve this multi-physics problem (3.6)–(3.15), a two-grid method is used on multiple domains, extending the approach presented in [25,27,36]. As illustrated in Fig. 3 (in two dimensions), the space discretization relies at each time step on:

(i) a coarse unstructured tetrahedral finite element discretization $\mathcal{T}_{h_{fe}}$ (with typical mesh size h_{fe} in the liquid region) of the whole domain $\Lambda \cup \Sigma$. At each time step, the discretization is refined in a neighborhood of the free surface and restricted a) to the metal domain $\Omega^n \cup \Sigma$ for the solution of the thermal problem, and b) to the liquid metal domain Ω^n only to solve the Stokes problem (3.8)–(3.9), both with finite elements.

(ii) a structured grid of smaller cells (with typical cell size h_{cells}) within the cavity Λ, used to solve the advection problems (3.10)–(3.12). More precisely, the cavity Λ is embedded into a parallelepiped box discretized into a structured Cartesian grid $\mathcal{C}_{h_{cells}}$, which is made out of small cells with a typical size h_{cells}.

Fig. 3, Step (1) shows the mesh refinement prior to the solution of the PDE problems. The dashed lines represent the new edges in the conforming finite element mesh created by the mesh refinement procedure. This interface tracking procedure allows to have a more accurate approximation of the free surface in order to apply surface forces. Based on the piecewise constant values of φ^{n+1} on the grid of small cells, we identify the cells on the interface ($0 < \varphi^{n+1} < 1$), and we construct the isosurface $\{\varphi^{n+1} = 0.5\}$. We identify all the edges of the finite element mesh that intersect the isosurface. Additional finite elements are constructed in order to keep a conforming finite element discretization.

The two-grid method allows to use a finer structured grid to increase the accuracy of the approximation of φ^{n+1}, and thus of the free surface Γ^{n+1}. The computational cost of solving parabolic problems (such as the Stokes problem) implicitly is kept reasonable by using a coarser finite element mesh. Following [36], we typically advocate $3 \leq h_{fe}/h_{cells} \leq 5$ for a reasonable trade-off between accuracy and computational efficiency.

This Eulerian approach is based on a volume-of-fluid method and fixed grids. Therefore it allows to tackle large deformations and changes of topologies. However, the deformations are expected to be rather small in the particular cases of laser melting/polishing processes that we consider in the sequel.
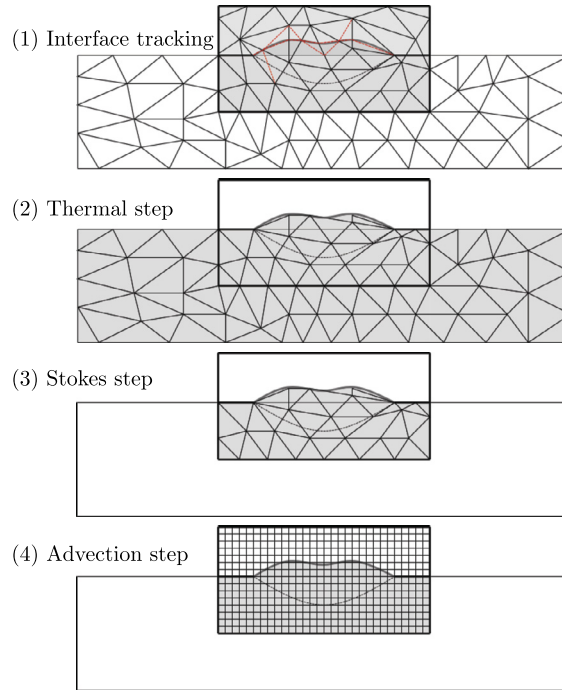
Fig. 3. Two-grid method (2D sketch). (1) The free surface is tracked with mesh adaptation techniques to have a more accurate approximation of the interface. The finite elements overlapping the free surface are cut and dashed lines represent the new created edges. The diffusion problems are solved on an unstructured finite element mesh of typical size h_{fe}, on embedded domains, for (2) the heat equation and (3) the Stokes problem respectively. (4) The advection problems are solved on a structured grid of small parallelepipedic cells of typical size h_{cells}. The shaded regions describe the computational domain for each step.

4.2. General space-discretized operator-splitting algorithm

More precisely, the complete space-discretized operator splitting algorithm reads as follows. At each time step, assuming that piecewise constant approximations of all variables are known on the structured grid of small cells, we proceed as follows:

(1) (Interface tracking) Construct an adapted finite element discretization of $\mathcal{T}_{h_{fe}}$ in order to obtain an accurate mesh approximation of the free surface. Details can be found in [26]. The restriction of this adapted mesh to $\Omega^n \cup \Sigma$ is used for solving the heat problem, and its restriction to Ω^n is used for solving the flow problem. The piecewise constant approximations of the variables are interpolated from the structured grid of small cells onto the space of piecewise linear finite elements. See [48] for more details.

(2) (Thermal step) Solve the heat problem with piecewise linear finite elements, in order to obtain predictions of the enthalpy $\mathcal{H}^{n+1/2}$ and temperature $T^{n+1/2}$ according to (3.3) (3.4) (3.5) [44].

(3) (Stokes step) Solve the Stokes problem (3.8) (3.9) with stabilized piecewise linear finite elements, in order to obtain a prediction of the velocity $\mathbf{v}^{n+1/2}$ and the pressure p^{n+1} [36]. The piecewise linear finite element approximations of all the unknowns are interpolated back onto the structured grid of small cells [48].

(4) (Advection step) Solve the advection problems with a forward characteristics method on the structured grid, in order to compute the corrections $\mathcal{H}^{n+1}, \mathbf{v}^{n+1}$ and φ^{n+1} according to (3.10)–(3.12). Numerical diffusion is controlled with a variation of the heuristic SLIC algorithm inspired by [35], and artificial compression of the fluid and mass conservation is ensured by post-processing techniques. Details can be found in [36].

This general operator-splitting algorithm is intrinsically sequential. However, all the parts that can be implemented in parallel have been parallelized via multithreading. For instance, the explicit advection step (the transport of cells), the interpolation operators, and the recalculation of mesh connectivity, have been parallelized. The mesh cutting procedures in the adaptive mesh refinement approach remain sequential.

Remark 3. From the theoretical standpoint, there is no stability limitation on the choice of the time step, since i) implicit finite elements schemes are used for both diffusion problems (Stokes and heat equation), and ii) the method of characteristics for the transport problem does not involve any stability criterion. All problems could be treated with different time steps, but, in the numerical experiments presented hereafter, the same time step is considered for the discretization of both
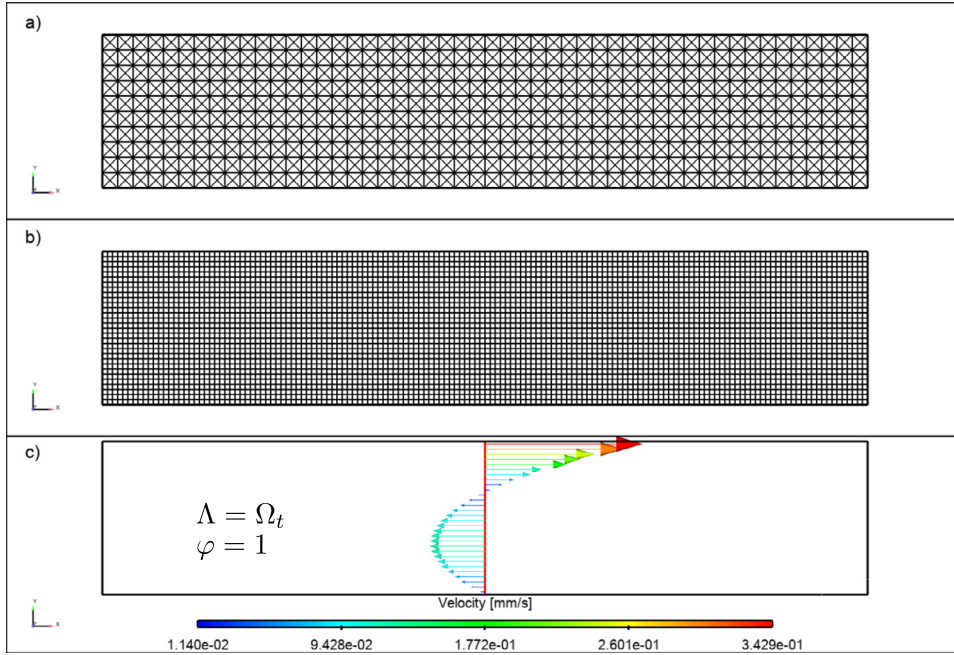
Fig. 4. Validation of the Marangoni effect without free surface: 2D sketch of the situation. a) the finite-element mesh; b) the structured grid; c) the velocity profile corresponding to (5.1).

Stokes and thermal operators. In practice, the final time of the simulation t_{max} is set first; then an adaptive time stepping algorithm is used in order to keep a CFL number between 1 and 5, and thus control the accuracy of the numerical scheme. The number of time steps for a simulation varies accordingly.

5. Numerical experiments

Numerical experiments are presented to validate the numerical methods with successive benchmark cases, to finally focus on the industrial processes of laser surface melting and polishing. The 2D simulations presented in this section are actually performed in a 3-dimensional domain that is very thin in one direction. In that case, we apply free-slip and adiabatic boundary conditions on the surfaces that are orthogonal to the pseudo-2D direction.

5.1. Marangoni effect without surface tension

The first benchmark test intends to validate the influence of the Marangoni effect without free surface and without coupling with thermal effects. We consider an infinite basin Λ (in the x- and z-directions) of height H (along the y-direction), with a linear surface tension coefficient $\gamma(x) = \gamma \cdot x$ imposed on the top surface ($y = H$).

Assuming free-slip boundary conditions on the top surface and no-slip conditions on the bottom surface, and taking the balance between capillary forces and viscous constraints into account, the analytical solution for the stationary velocity can be expressed as

$$\mathbf{v} = \frac{\gamma H}{2\mu} \left(\frac{3}{2} \left(\frac{y}{H} \right)^2 - \frac{y}{H} \right) \mathbf{e}_x \tag{5.1}$$

which is the superposition of a Poiseuille flow with a shear flow [31]. In the context of Fig. 1, we thus have $\Sigma = \emptyset, \Gamma_t = \emptyset$ and $\Lambda = \Omega_t$.

The numerical setup is as follows. We consider a cavity $\Lambda = [0, 5H] \times [0, H] \times [0, h_{fe}]$ of height $H = 4$[mm] and (structured) isotropic finite-element meshes with $N = 10, 20, 40$ and 80 elements along the y-direction (see Fig. 4.a). Thus we have $h_{fe} = H/N$ and we consider a Cartesian grid such that $h_{cells} = \frac{1}{3} h_{fe}$ (see Fig. 4.b). Free-slip boundary conditions are imposed on the top surface, as well as on front and back surfaces, while no-slip boundary conditions are enforced on the rest of the boundary. The cavity is filled with liquid aluminum, whose mass density and dynamic viscosity are respectively given by $\rho = 2.385 \cdot 10^{-6}$[kg mm^{-3}] and $\mu = 1.3 \cdot 10^{-3}$[kg mm^{-1} s^{-1}]. The convergence of the velocity profiles is illustrated in Fig. 5. Fig. 6 shows the first order convergence of the error on the approximation of the velocity as a function of the mesh size.
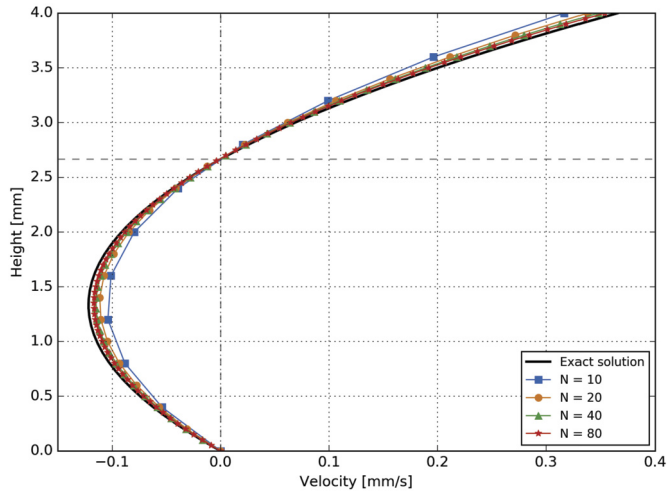
Fig. 5. Validation of the Marangoni effect without free surface: convergence of velocity profiles.
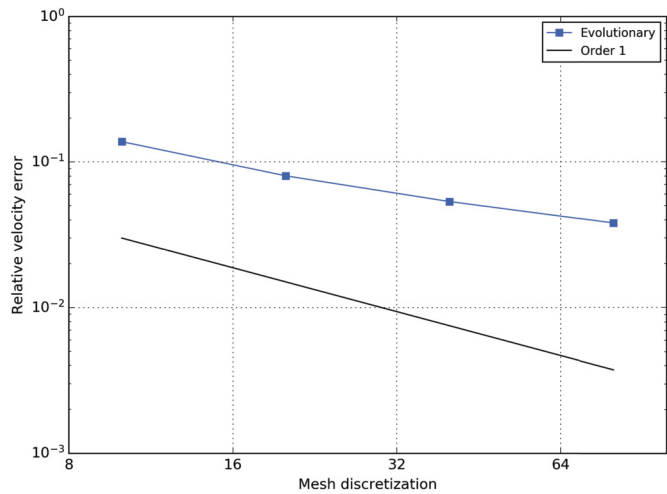

**Fig. 6.** Validation of the Marangoni effects without free surface: convergence order.

5.2. Convection-driven cavity: tin melting front

The purpose of the second, classical, numerical experiment is to validate the coupling between the Navier-Stokes equations and the heat equation without free surface. A squared cavity is filled with liquid and solid tin, and is subjected to a temperature difference between its left and right boundaries. The liquid region is set into motion by the natural convection force $\mathbf{f}(T) = -\rho \mathbf{g} \lambda (T - T_f)$, where λ is the thermal expansion coefficient and T_f is the temperature of fusion. The induced flow influences the solidification front, which in turn modifies the liquid region, until a stationary solution is reached. In the context of Fig. 1, we have $\Sigma = \emptyset$, $\Gamma_t = \emptyset$ and $\Omega_t = \Lambda = [0, 0.1] \times [0, 0.1] \times [0, h_{fe}]$ for all $t \in (0, t_{max})$. Fig. 7 illustrates a 2D sketch of the situation in the xy-plane.

We consider (structured) finite-element meshes with $N = 16, 32, 64, 128$ and 256 elements per side. Thus we have $h_{fe} = 0.1/N$ and we consider a Cartesian grid such that $h_{cells} = \frac{1}{3} h_{fe}$. The time step is constant and set to $\tau^n = 8/N$, and the simulation is performed until $t_{max} = 120[s]$. Fixed temperatures $T_{hot} = 508[K]$ and $T_{cold} = 503[K]$ are respectively imposed on the left and right boundaries, whereas adiabatic boundary conditions are imposed on other surfaces. For the Stokes problem, free-slip conditions are applied on the front and back surfaces to account for the pseudo-2D approximation, and no-slip conditions are applied on the rest of the boundary. The solidification process is modeled through the reaction term (2.3) (with $\bar{\alpha} = 1$ and $\varepsilon = 10^{-3}$). The physical properties of the material are listed in Table 1.

At initial time, we assume a uniform temperature gradient and zero velocity. Fig. 8 illustrates the evolution of the velocity field and solid front, while Fig. 9 illustrates the stationary velocity and temperature fields.

A convergence study of the algorithm is then undertaken. Fig. 10 illustrates the position of the solidification front for various mesh discretizations. We observe that the approximation of the solidification front converges when the discretization
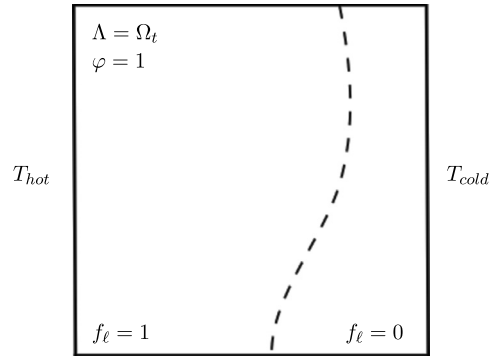
Fig. 7. Tin melting front: 2D sketch of the situation. A square cavity containing both liquid and solid tin is subjected to a temperature difference between the left and right boundaries.
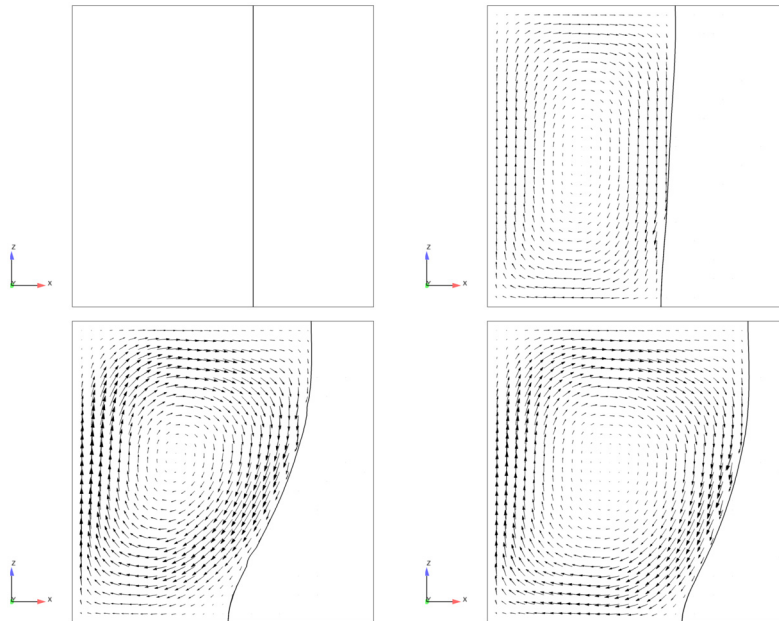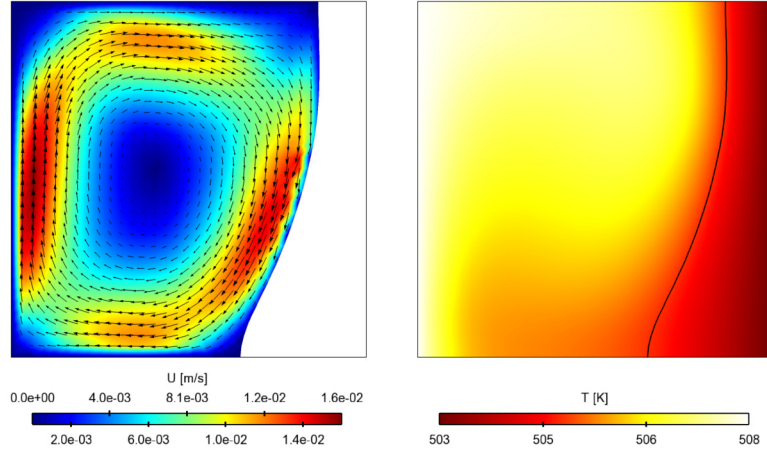

Fig. 8. Tin melting front. Snapshots of the numerical approximation of the velocity solution at time $t = 0, 4, 16$ and $120[s]$ (from left to right, top to bottom), when $N = 32$, together with the solidification interface.

Table 1
Tin melting front: Physical properties of the considered material.

Property	Symbol	Value	Units
Density	ρ	7500	$kg\,m^{-3}$
Dynamic viscosity	μ	$6 \cdot 10^{-3}$	$kg\,m^{-1}\,s$
Specific heat capacity	C_p	200	$J\,kg^{-1}\,K^{-1}$
Thermal conductivity	k	60	$W\,m^{-1}\,K^{-1}$
Thermal expansion	λ	$2.67 \cdot 10^{-4}$	–
Latent heat of fusion	L	60000	$J\,kg^{-1}$
Temperature of fusion	T_f	505	K

parameters go to zero. Moreover, a comparison with the solution obtained with the COMSOL© software is illustrated (black line). The COMSOL simulation is based on the "Marangoni effect" test case, which can be publicly found in the application gallery on the company web site [49]. The test case is based on coupled physics (so-called *Laminar Flow (CFD)* and *Heat transfer in fluid*), and the multiphysics coupling is performed through the *no-isothermal flow* with *Marangoni effect* laws. The standard segregated solver is used for the resolution. We observe that the approximation of the solidification front converges when the discretization parameters go to zero, and compares well with the solution obtained with the COMSOL© software (black line) [49].

Fig. 9. Tin melting front. Snapshot of the numerical approximation of the velocity (left) and temperature (right) at the stationary stage ($N = 32$).
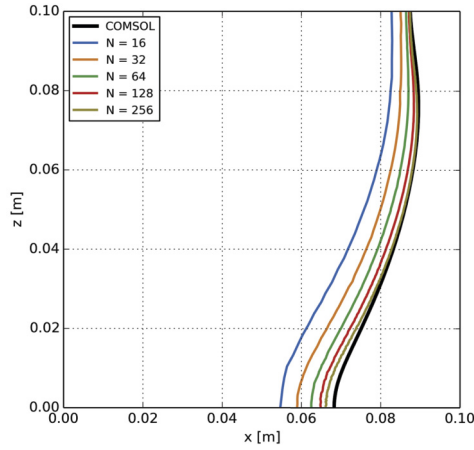
Fig. 10. Tin melting front. Position of the solidification front for different mesh discretizations and comparison with the numerical solution obtained with COMSOL® (see [49]).

Finally, we consider the numerical solution obtained with $N = 256$ as the exact solution, and compare it with the results obtained with coarser meshes. Fig. 11 visualizes the convergence of the relative error in L^2-norm of various numerical quantities, which exhibit the expected order one convergence rate.
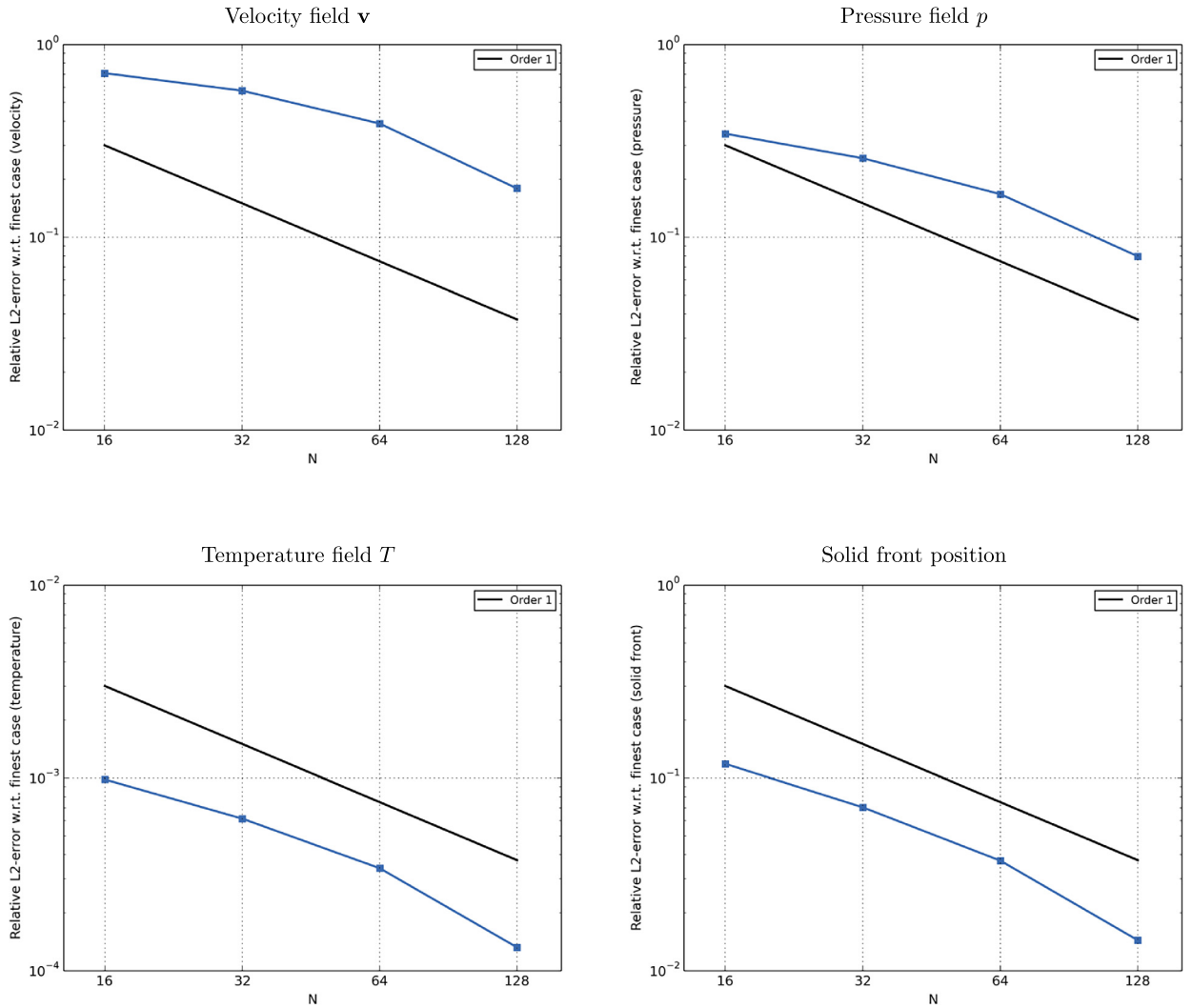
5.3. 2D static laser melting

This numerical experiment consists of a single static laser source melting a piece of metal [32,50] in a 2D configuration. It allows to validate the full coupling between flow and heat equations with Marangoni effects on the free surface.

The setup is that of Fig. 1, with $\Lambda = [-2.5, 2.5] \times [0, h_{fe}] \times [4.6, 8]$ [mm]. We start the simulation with a flat free surface such that $\Sigma \cup \Omega_0 = [-7, 7] \times [0, h_{fe}] \times [0, 7]$ [mm], where $h_{fe} = 5/N$ is the finite-element mesh size, for $N = 24, 48, 96$ and 192. Fig. 12 illustrates the spatial discretization. The finite element mesh is finer in Λ and coarser towards the boundary $\partial \Sigma \setminus \partial \Lambda$. The structured Cartesian grid defined over Λ is such that $h_{cells} = \frac{1}{3} h_{fe}$ [mm].

We consider the Böhler S705 steel as material, whose physical properties are listed in Table 2. The surface tension coefficient depends on the temperature, and thus induces a specific melting pool shape through Marangoni effects. Fig. 13 shows the derivative of the surface tension coefficient $\gamma'(T)$ for two different sulfur densities (see [31,50,51] for more details). The numerical results presented hereafter are obtained with the curve corresponding to a sulfur density of 150 [ppm]. The enthalpy-temperature relation $T = \beta(\mathcal{H})$ is taken as in [44].

The static laser source is considered as a beam of radius $R = 1.4$ [mm] with a power of $P = 5200$ [W]. It is modeled by a heat flux boundary condition (where heat loss is neglected) given by

$$k \frac{\partial T}{\partial \mathbf{n}_{\Gamma_t}} = \begin{cases} \dfrac{C \eta P}{\pi R^2} & |x| \leq R \\ 0 & |x| > R \end{cases} \quad \text{on } \Gamma_t, \tag{5.2}$$

Fig. 11. Tin melting front. L^2-errors with respect to the finest mesh ($N = 128$) of: the velocity field **v** (top left); the pressure field p (top right); the temperature field T (bottom left); the solid front position (bottom right).
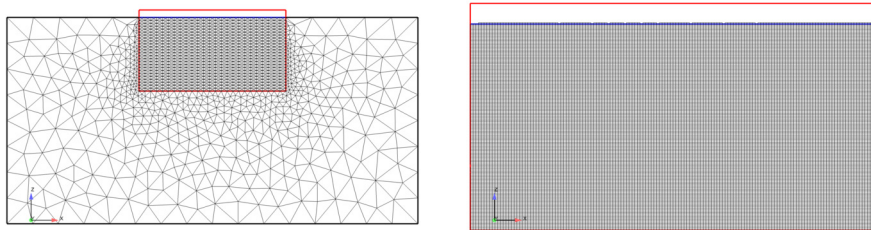
Fig. 12. 2D static laser melting. Computational domains: Left: an unstructured finite element mesh at $t = 0$, which is finer in a neighborhood of the laser impact (red rectangle domain) and coarser further away from the melting zone. Right: a structured grid of small, regular, rectangle, cells, which covers the domain in the neighborhood of the laser impact ($N = 48$ in both cases).

where x denotes the horizontal distance, $\eta = 0.13$ [–] is the metal absorption coefficient and $C = 0.2$ is a constant to account for the pseudo-2D approximation. Adiabatic boundary conditions are imposed on the remaining parts of the boundary. The initial condition for the heat problem is the ambient temperature, such that $f_\ell \equiv 0$ in Ω_0 (no liquid region).

For this kind of problem the gravitational forces can be neglected compared to surface tension forces (small Bond number). The coefficients in (2.3) are taken as $\bar{\alpha} = 100$ and $\varepsilon = 10^{-3}$. We apply slip boundary conditions in the xz-planes, no-slip boundary conditions on $\partial \Lambda$ and the natural force condition on the free surface Γ_t. The initial condition for the velocity is $\mathbf{v} \equiv \mathbf{0}$.
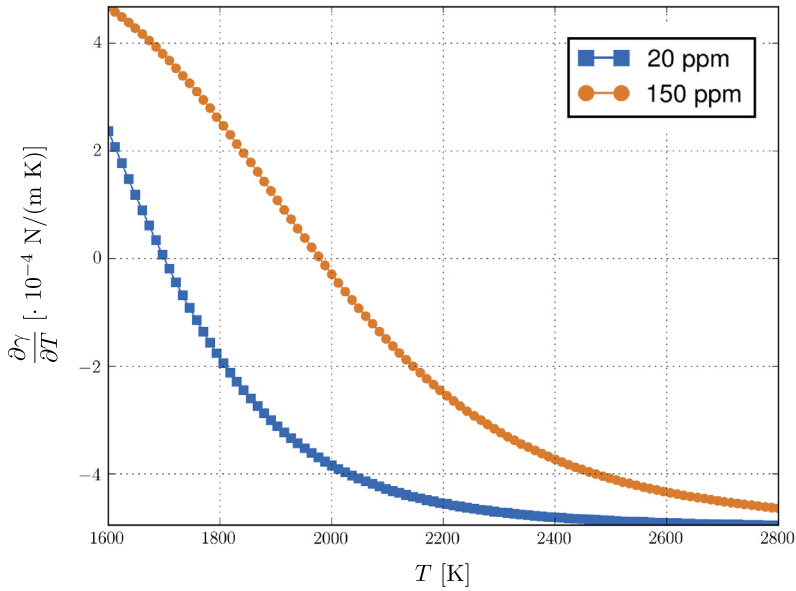
Fig. 13. Variation of surface tension versus temperature ($\gamma'(T)$) for two samples of S705 steel containing 20 and 150 [ppm] of sulfur, respectively.

Table 2
Material properties for Böhler S705 steel.

Property	Symbol	Value	Units
Density	ρ	8100	kg/m^3
Temperature of fusion	T_f	1620	K
Dynamic viscosity	μ	0.006	kg/(m.s)
Thermal conductivity of solid	k_s	22.9	J/(m.s.K)
Thermal conductivity of liquid	k_l	22.9	J/(m.s.K)
Specific heat of solid	C_{p_s}	627	J/(kg.K)
Specific heat of liquid	C_{p_l}	723.14	J/(kg.K)
Latent heat of fusion	L	2.508e+5	J/kg

Table 3
2D static laser melting. Average CPU time by time step. The remaining CPU time is mostly used for interface tracking and interpolation between grids.

N	CPU time [min/time step]	Heat [%]	Stokes [%]	Convection [%]
24	0.16	2	81	1
48	0.39	3	75	1
96	1.60	3	77	1
192	8.55	2	82	1

Fig. 14 illustrates the solution after $t_{max} = 0.15$ [s], namely the liquid fraction, the temperature and the velocity streamlines. Numerical experiments show a strong coupling between the thermal aspects and the deformation of the free surface, as well as internal currents in the melt pool which are due to the Marangoni effect.

Fig. 15 shows the convergence behavior of the algorithm for four mesh sizes.

Table 3 summaries the average CPU time by iteration for each mesh discretization, and for the three main simulation steps.

5.4. 3D static laser melting

This numerical example revisits the one of Section 5.3 in a real 3D configuration. The goal of this test case is to highlight the influence of the derivative $\gamma'(T)$ on the melt pool shape, and the effects of these variations on the free surface. Such a test case has been presented in [50,51] but only for a flat surface. Therefore, we start by presenting the results obtained with a flat surface before introducing the coupling with a free surface in a second step.

The sample geometry is a cylinder of radius 15 [mm] and thickness 15 [mm]. We use the same approach as in Section 5.3 to define the computational domains. The same material is used (see Table 2) and two sets of simulations are carried out using the 20 and 150 [ppm] sulfur density curves for $\gamma'(T)$ (see Fig. 13). The surface tension coefficient changes with
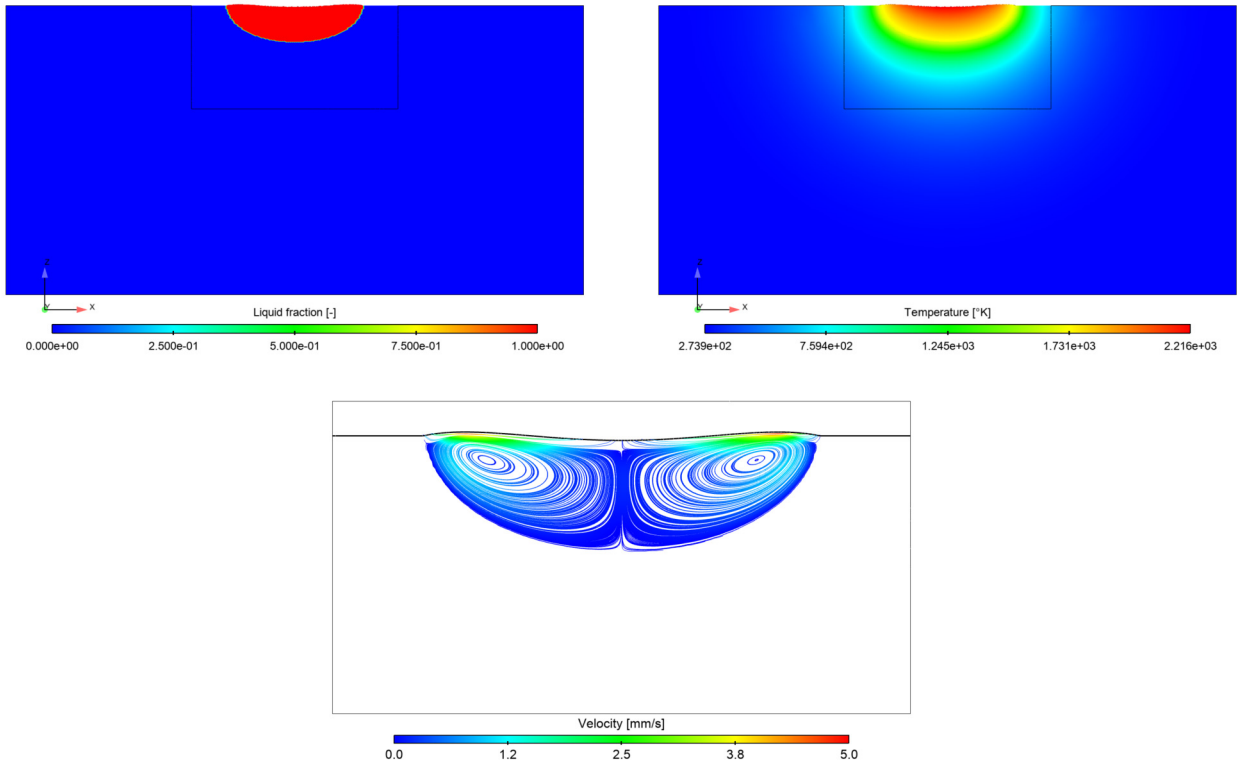
Fig. 14. 2D static laser melting. Snapshots at time $t = 0.15$ [s] of the numerical approximation of: the liquid fraction f_ℓ (top left); the temperature T (top right); the velocity streamlines (bottom).
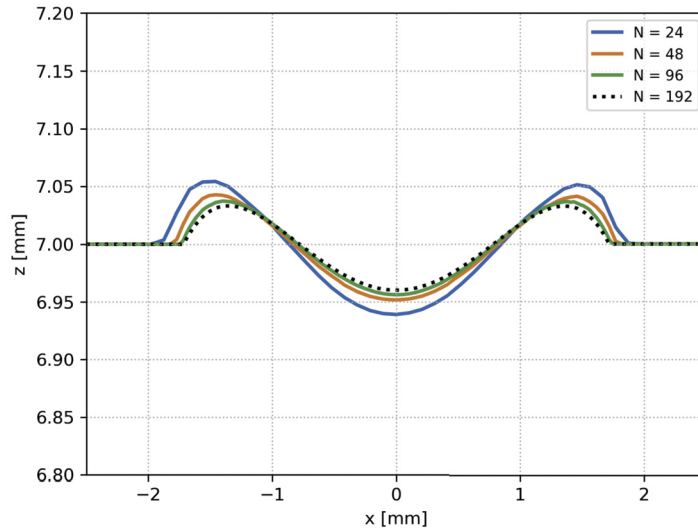

Fig. 15. 2D static laser melting. Free surface deformations for different mesh sizes.

temperature, due to the active sulfur concentrations present in the steel. The simulation and laser parameters are identical to those presented in Section 5.3, except that $C = 1$ [–] in the 3-dimensional case.

We first present the results obtained with a flat interface, at time $t = 1.5$ [s]. Fig. 16 shows the temperature field and the solidification fronts obtained with the two variants of the curve $\gamma'(T)$. In particular, we observe that the radial symmetry is strictly respected. Fig. 17 shows the velocity field together with velocity and temperature profiles along the marked vertical red line. We observe that the orientation of the velocity changes in the radial direction depending on the sulfur concentration.
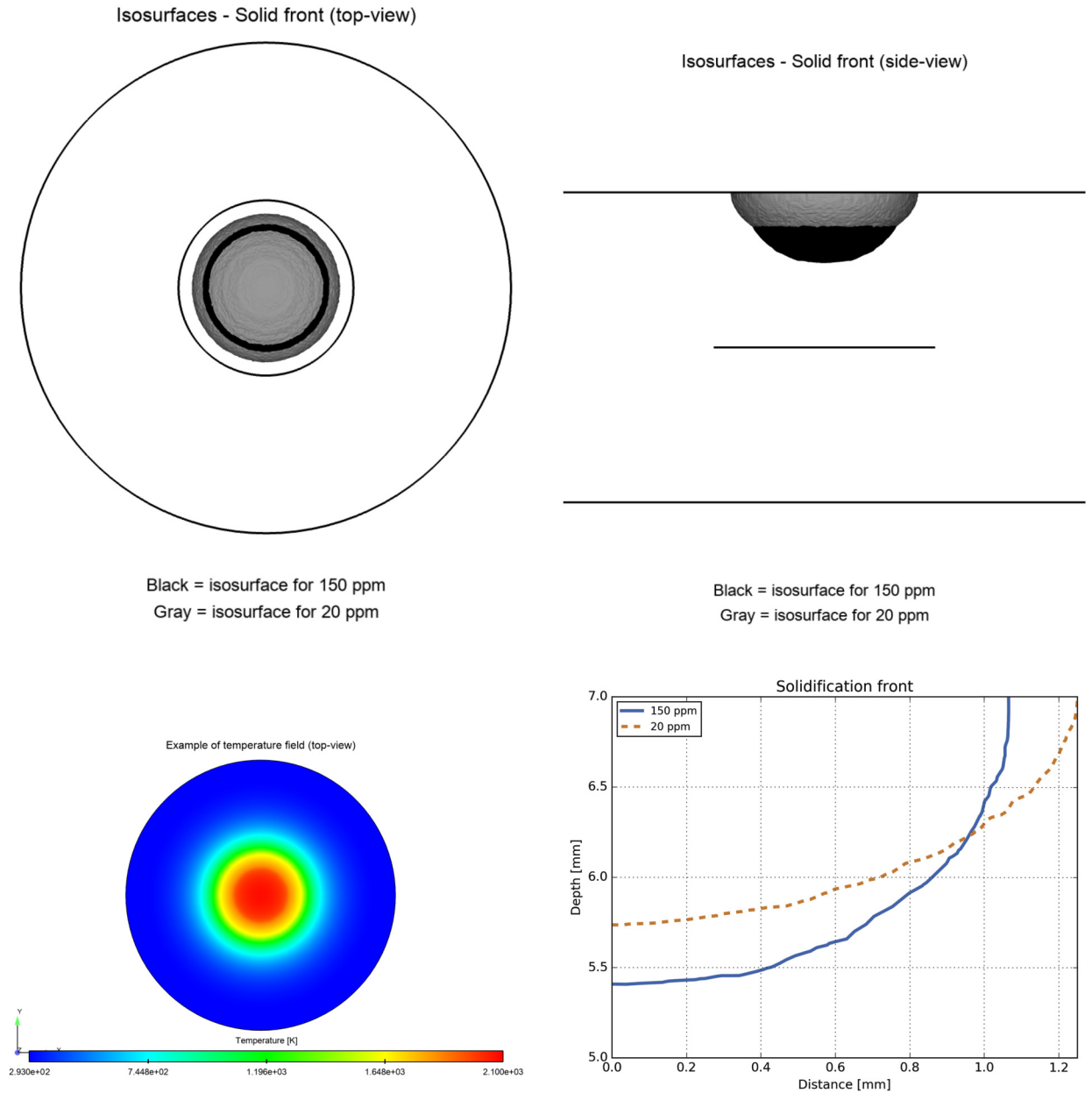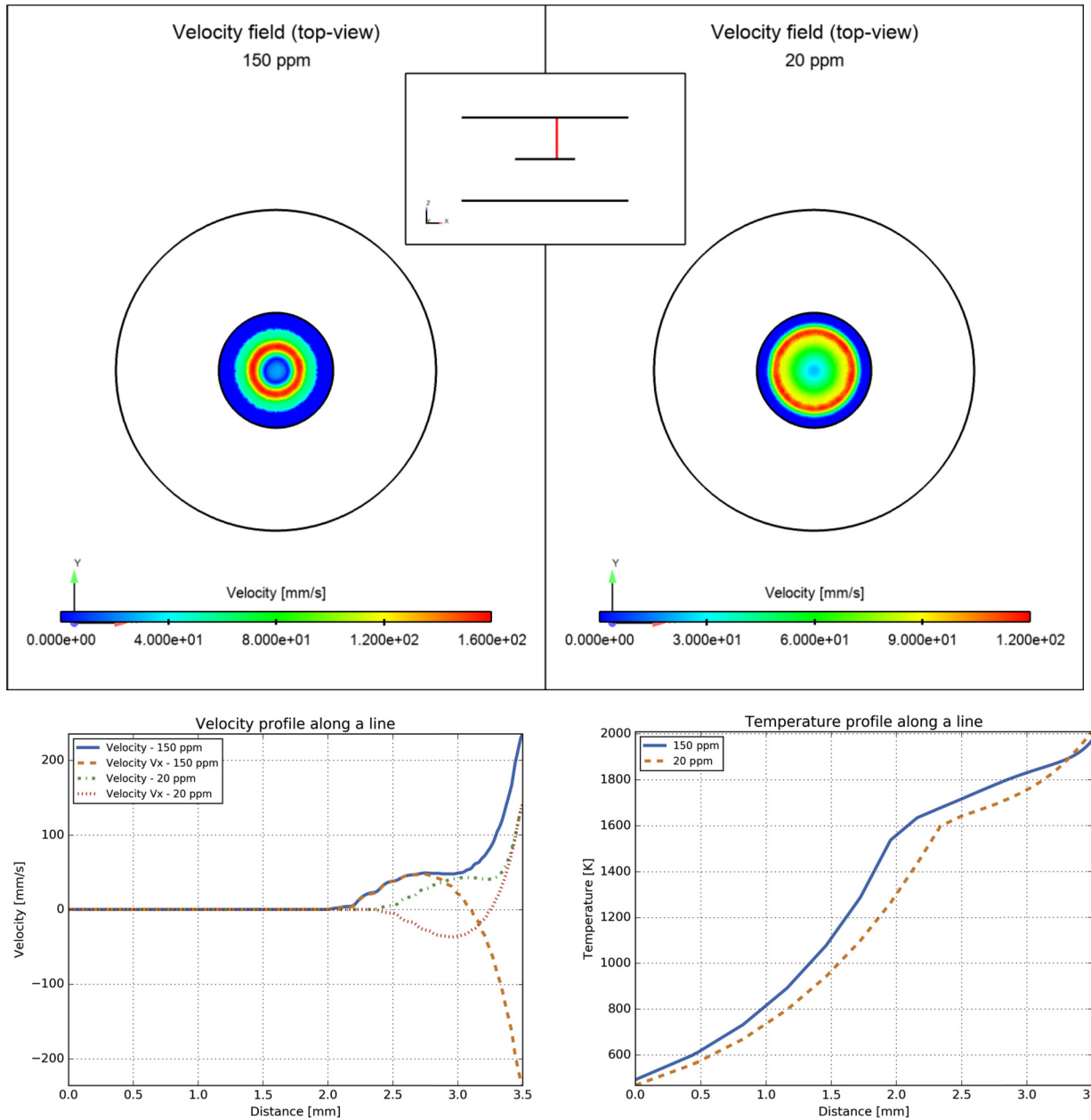
Fig. 16. 3D static laser melting. Snapshots of the numerical solution (with flat interface) at time $t = 1.5$ [s]: the solidification front from top view (top left); the solidification front on a radial cutting plane (top right); the temperature field from top view (bottom left); the solidification front from side view (bottom right).

In a second step, we present numerical results obtained when considering a free surface, also at time $t = 1.5$ [s]. Fig. 18 shows the free surface deformation and transversal profiles for each variant of the surface tension coefficient. We observe that the shape of the free surface is closely related to the sulfur concentration. Fig. 19 shows a comparison of solidification fronts for the two surface tension coefficients, considering the solutions corresponding to a flat surface or a free surface respectively. The results confirm that taking into account a free surface for such a process has no significant effect on the weld pool topology.

5.5. 3D dynamic laser polishing

A final example of surface laser polishing is presented, to qualitatively illustrate the potential of numerical simulations to reproduce all effects involved in such a complicated experimental process. The setup is $\Sigma \subset (-7.5, 7.5) \times (-7.5, 12.5) \times (0, 8)$ [mm] and $\Lambda = (-0.75, 0.75) \times (0, 5) \times (7.85, 8.3)$ [mm]. The initial free surface Γ_0 has a random roughness of typically

Fig. 17. 3D static laser melting. Snapshots of the numerical solution (with flat interface) at time $t = 1.5$ [s]: the velocity field (150 [ppm]) from top view (top left); the velocity field (20 [ppm]) from top view (top right); the velocity profiles along the red line (bottom left); the temperature profiles along the red line (bottom right).

50 [µm], as illustrated in Fig. 20. The thermal solution is computed in the metal domain $\Sigma \cup \Omega_t$, which is chosen large enough to account for the temperature diffusion. The flow problem is solved in $\Omega_t \subset \Lambda$, which corresponds to the area swept by the laser. This multi-domain approach is essential for the efficient simulation of such processes in such configurations.

Fig. 21 illustrates the spatial discretization. The finite element mesh is finer ($h_{fe} = 0.025$ [mm]) in Λ and coarser ($h_{fe} = 1$ [mm]) towards the boundary $\partial \Sigma \setminus \partial \Lambda$. The structured Cartesian grid defined over Λ is such that $h_{cells} \cong 5 \cdot 10^{-3}$ [mm].

We consider the X38CrMVo5-1 steel, whose physical properties are listed in Table 4. The variation of the temperature and thermal conductivity with respect to enthalpy are given in Fig. 22.

The laser source is considered as a beam of radius $R = 0.45$ [mm] with a power of $P = 410$ [W]. It is modeled by a heat flux boundary condition with top hat profile such as (5.2) (on Γ_t), moving along the y-direction with a velocity of 35 [mm/s]. We consider a metal absorptivity of $\eta = 0.20$ [–]. Adiabatic boundary conditions are imposed on the rest of the boundary. The initial condition for the heat problem is the ambient temperature (no liquid region).
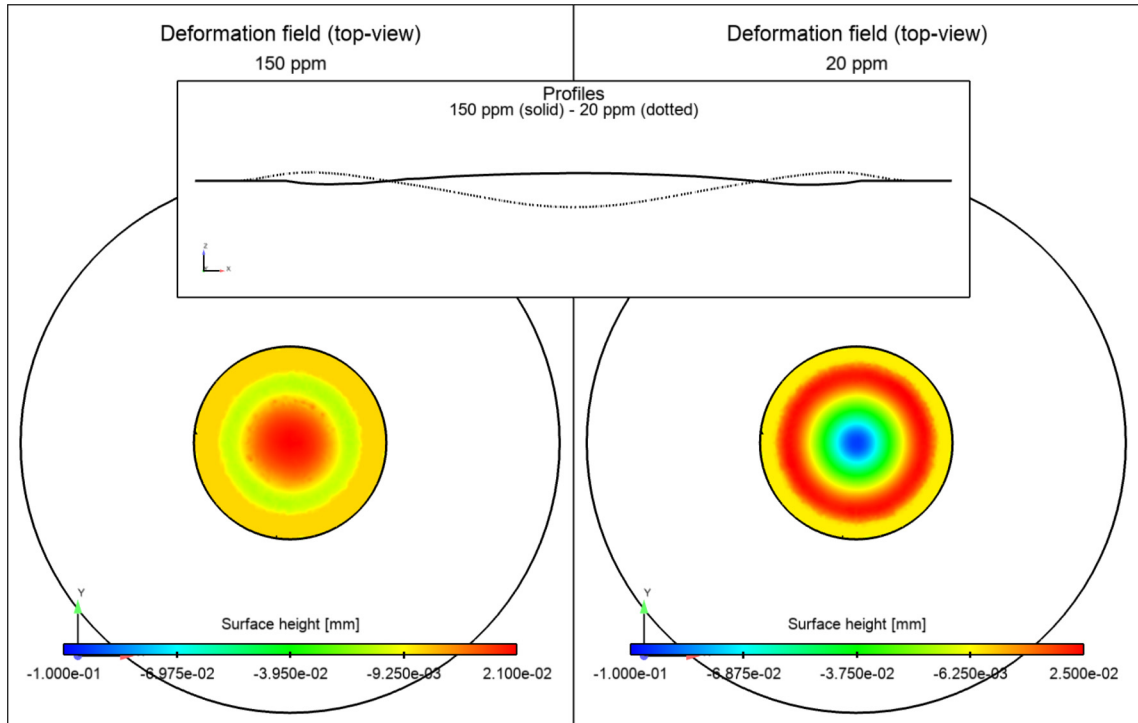
Fig. 18. 3D static laser melting. Snapshots of the numerical solution (with free surface) at time $t = 1.5$ [s]: the free surface deformation (150 [ppm]) from top view (left); the free surface deformation (20 [ppm]) from top view (right); the free surface profiles along a transversal line (top center).
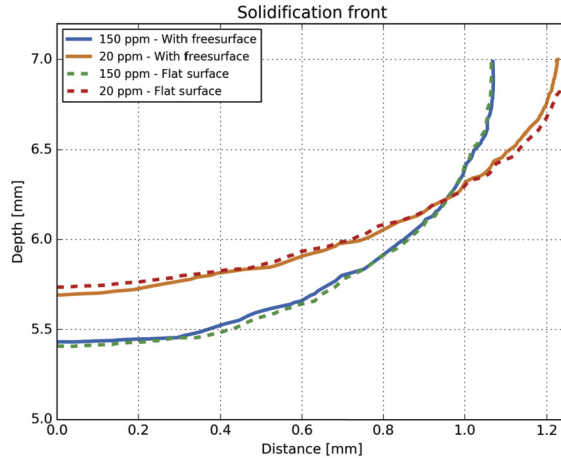
Fig. 19. Comparison of solidification fronts (weld pool topology) obtained with flat (dotted lines) or free surface (solid lines) and with surface tension equivalent to 150 [ppm] respectively 20 [ppm].

For the Stokes problem, gravity is neglected, which is a valid assumption for small Bond numbers. The coefficients in (2.3) are taken as $\bar{\alpha} = 100$ and $\varepsilon = 10^{-3}$. We apply no-slip boundary conditions on $\partial \Lambda$ and the force condition (2.7) on the free surface Γ_t. The initial velocity is zero.

Figs. 23–25 show the results before ($t = 0$) and after ($t_{max} = 0.1$ [s]) a single laser sweep. The effect of polishing is highlighted along longitudinal and transversal cuts of the free surface. The longitudinal cut in Fig. 24 exhibits an expected small bulge a little further than the final position of the laser, which corresponds to the liquid pushed at the front of the laser displacement. Since the piece of metal is at ambient temperature at initial time, the laser has already moved a little when the melt pool reaches its characteristic size. For $y \geq 1.5$[mm], we observe a significant decrease of roughness on the laser track. On the transversal cuts in Fig. 25, the effect of polishing is local at the center of the laser spot and again a significant decrease of roughness is observed in the middle spot. Moreover, bulges appear on each side of the laser track,
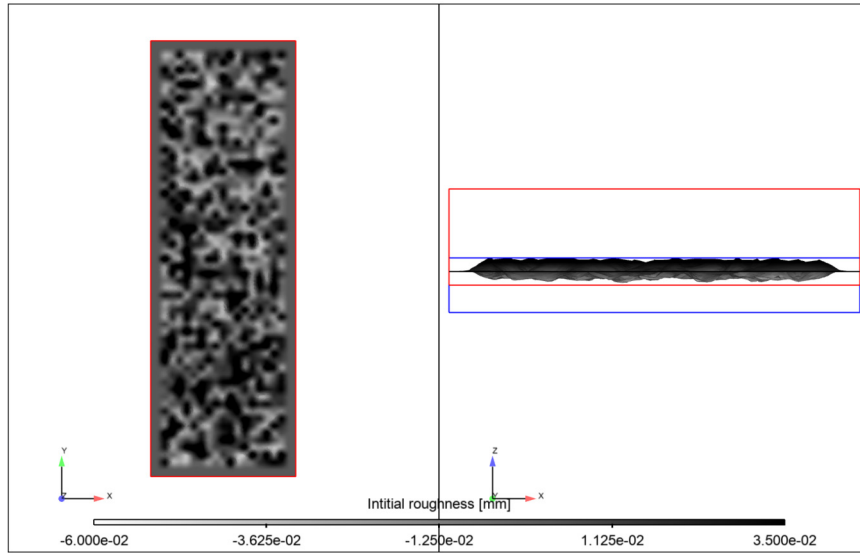
Fig. 20. 3D dynamic laser polishing. Top view and side view of the initial rough free surface in the computational domain Λ.
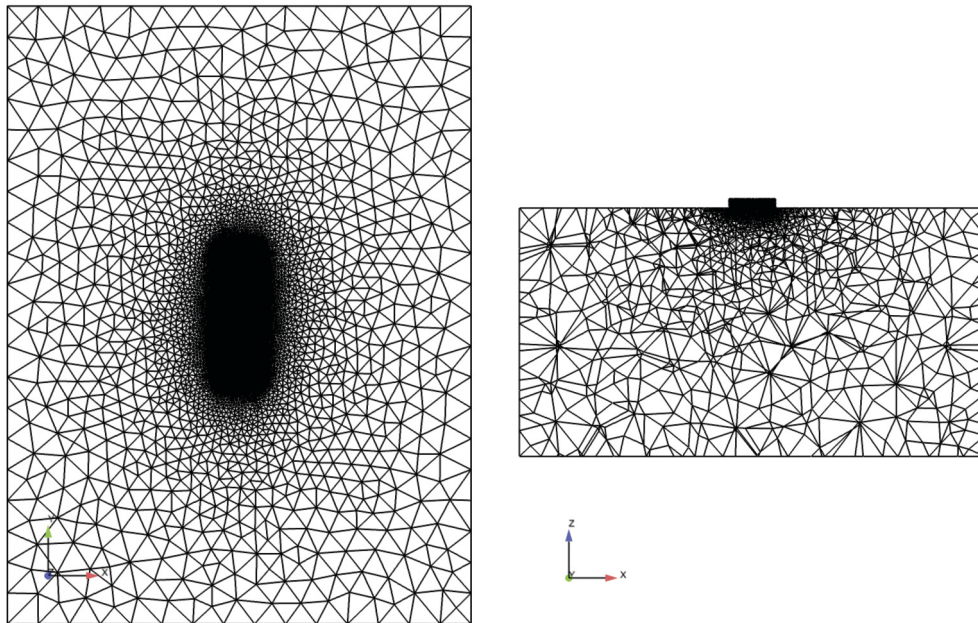

Fig. 21. 3D dynamic laser polishing. Top view of the finite element mesh for Σ ∪ Λ (left); side view of the finite element mesh for Σ ∪ Λ on the cutting plane $y \equiv 2.5$ (right).

which shows that many laser passes, with overlaps, will be needed to obtain a smooth surface finish after the polishing process.

6. Conclusion and perspectives

A numerical method relying on a multi-domain approach, together with a splitting algorithm and a multi-grid discretization has been presented to simulate laser melting and polishing processes. The results show the correct implementation and the potential of our approach to simulate such coupled problems involving thermal aspects with phase transitions and fluid dynamics computations. Furthermore, the effects of surface tension, including the Marangoni effect, have been highlighted. The final numerical experiments point out that all effects can be taken into account in 3D simulations. For the laser polishing process, numerical simulations may help to understand the influence of process parameters (such as laser size, power and velocity), but also that of material properties (e.g. initial roughness, surface tension coefficient and its variation

Table 4
Material properties for X38CrMVo5-1 steel.

| Property	Symbol	Value	Units
Density	ρ	7600	kg/m^3
Temperature of fusion	T_f	1505	K
Dynamic viscosity	μ	4.94e-4	kg/(m.s)
Specific heat of solid	C_{p_s}	590	J/(kg.K)
Latent heat of fusion	L	2.47e+5	J/kg
Surface tension	γ	2.809 - 7.4e-4*T	N/m
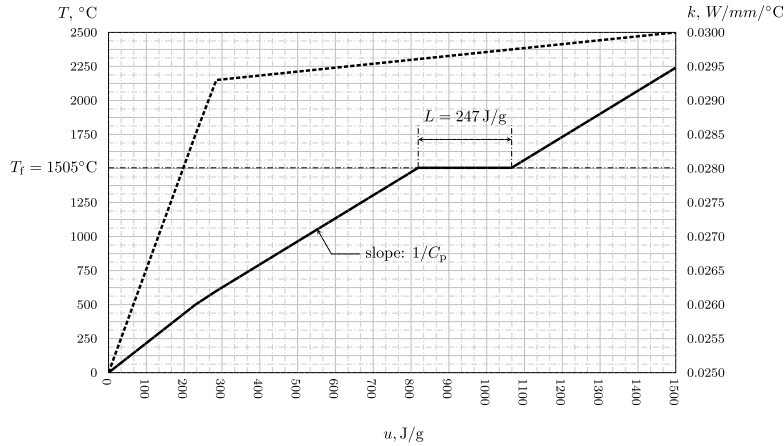
Fig. 22. Temperature T (continuous line) and thermal conductivity k (dotted line) as a function of the specific enthalpy for the X38CrMVo5-1 steel.
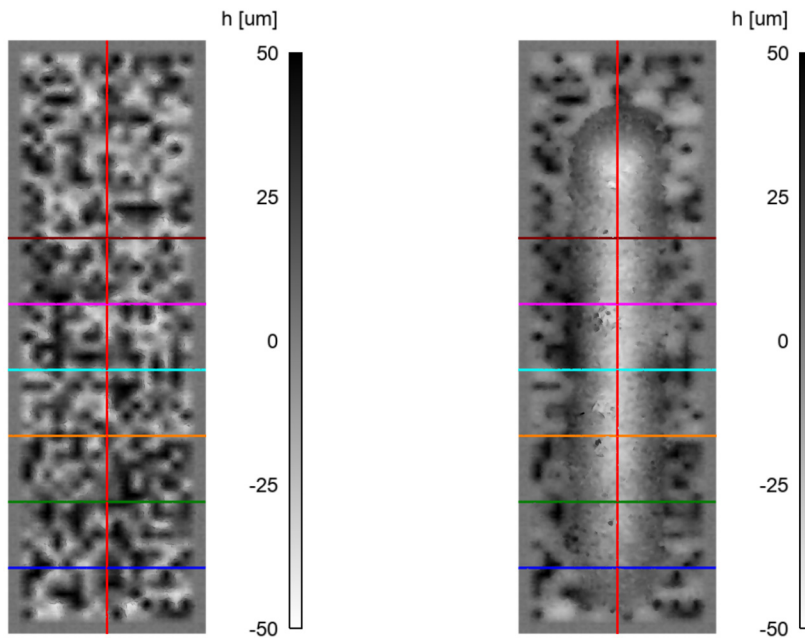

Fig. 23. 3D dynamic laser polishing. Initial free surface roughness (left) and polishing result after the laser treatment (right), with highlighted lines corresponding to the deformation profiles in Fig. 24 and Fig. 25.

with temperature, components of alloyed steel, etc.). Since the laser polishing process market is growing, especially because it is used to polish parts produced with additive manufacturing, future perspectives are to apply the numerical model to industrial applications.
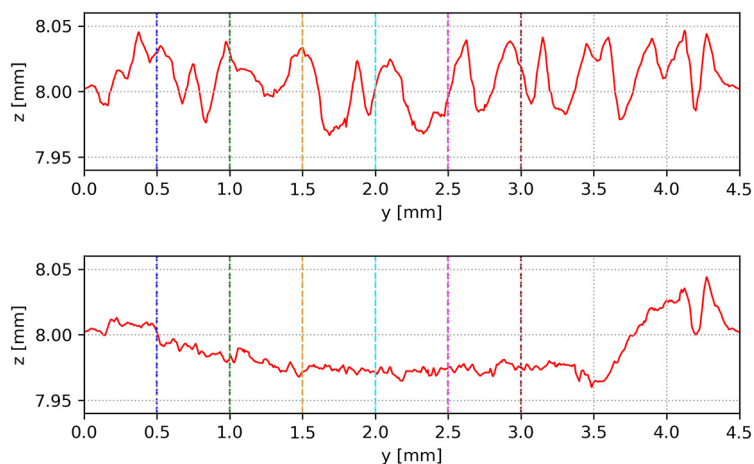
Fig. 24. 3D dynamic laser polishing. Longitudinal deformation profile at $t = 0$[s] (top) and $t = 0.1$[s] (bottom). The vertical dashed lines correspond to transversal profiles in Fig. 25.
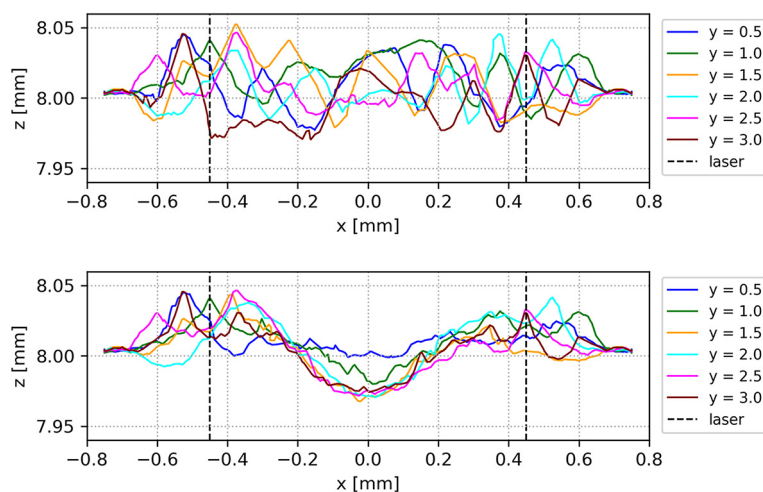
Fig. 25. 3D dynamic laser polishing. Transversal deformation profiles at $t = 0$[s] (top) and $t = 0.1$[s] (bottom). The vertical dashed lines represent the laser diameter.

CRediT authorship contribution statement

Alexandre Caboussat: Conceptualization, Methodology, Project administration, Supervision, Writing – original draft, Writing – review & editing. **Julien Hess:** Investigation, Methodology, Software, Validation, Visualization, Writing – original draft. **Alexandre Masserey:** Investigation, Software, Validation, Visualization. **Marco Picasso:** Conceptualization, Supervision.

Declaration of competing interest

The authors declare that they have no known competing financial interests or personal relationships that could have appeared to influence the work reported in this paper.

Data availability

Data will be made available on request.

Acknowledgements

References

[1] F.F. Bownes, Sand Casting, Macmillan Education UK, London, 1971, pp. 63–74.

[2] N. Kalentics, E. Boillat, P. Peyre, C. Gorny, C. Kenel, C. Leinenbach, J. Jhabvala, R.E. Logé, 3d laser shock peening – a new method for the 3d control of residual stresses in selective laser melting, Mater. Des. 130 (2017) 350–356, https://doi.org/10.1016/j.matdes.2017.05.083.

[3] D.M. Stefanescu, G. Upadhya, D. Bandyopadhyay, Heat transfer-solidification kinetics modeling of solidification of castings, Metall. Trans. A 21 (3) (1990) 997–1005, https://doi.org/10.1007/BF02656584.

[4] A. Temmler, E. Willenborg, K. Wissenbach, Laser polishing, Proc. SPIE Int. Soc. Opt. Eng. 8243 (2012) 19, https://doi.org/10.1117/12.906001.

[5] E.V. Bordatchev, A.M.K. Hafiz, O.R. Tutunea-Fatan, Performance of laser polishing in finishing of metallic surfaces, Int. J. Adv. Manuf. Technol. 73 (1–4) (2014) 35–52.

[6] E. Willenborg, Process fundamentals and industrial applications of laser polishing, in: 2nd Conference on Laser Polishing, LaP, Aachen, Germany, 2016.

[7] S. Kolossov, E. Boillat, R. Glardon, P. Fischer, M. Locher, 3D FE simulation for temperature evolution in the selective laser sintering process, Int. J. Mach. Tools Manuf. 44 (2) (2004) 117–123, https://doi.org/10.1016/j.ijmachtools.2003.10.019.

[8] A. Krishnan, F. Fang, Review on mechanism and process of surface polishing using lasers, Front. Mech. Eng. 14 (3) (2019) 299–319, https://doi.org/10.1007/s11465-019-0535-0.

[9] E. Bordatchev, S. Cvijanovic, O.R. Tutunea-Fatan, Effect of initial surface topography during laser polishing process: statistical analysis, Proc. Manuf. 34 (2019) 269–274, https://doi.org/10.1016/j.promfg.2019.06.150, 47th SME North American Manufacturing Research Conference, NAMRC 47, Pennsylvania, USA.

[10] Y.A. Mayi, M. Dal, P. Peyre, R. Fabbro, A mesoscopic approach for modelling laser beam melting (LBM), in: II International Conference on Simulation for Additive Manufacturing, 2019.

[11] T.V. Vu, G. Tryggvason, S. Homma, J.C. Wells, Numerical investigations of drop solidification on a cold plate in the presence of volume change, Int. J. Multiph. Flow 76 (2015) 73–85.

[12] Y.A. Mayi, M. Dal, P. Peyre, R. Fabbro, Two-phase flow modelling of metal vaporisation under static laser shot using a double domain ale method – a feasibility study, in: 2018 COMSOL Conference, 2018.

[13] S. Ancellotti, V. Fontanari, A. Molinari, E. Iacob, P. Bellutti, V. Luchin, G. Zappini, M. Benedetti, Numerical/experimental strategies to infer enhanced liquid thermal conductivity and roughness in laser powder-bed fusion processes, Addit. Manuf. 27 (2019) 552–564, https://doi.org/10.1016/j.addma.2019.04.007.

[14] L. Moniz, Q. Chen, G. Guillemot, M. Bellet, C.-A. Gandin, C. Colin, J.-D. Bartout, M.-H. Berger, Additive manufacturing of an oxide ceramic by laser beam melting—comparison between finite element simulation and experimental results, J. Mater. Process. Technol. 270 (2019) 106–117, https://doi.org/10.1016/j.jmatprotec.2019.02.004.

[15] A. Paolini, S. Kollmannsberger, E. Rank, Additive manufacturing in construction: a review on processes, applications, and digital planning methods, Addit. Manuf. 30 (2019) 100894, https://doi.org/10.1016/j.addma.2019.100894.

[16] B. Wucher, L. Arbaoui, Multiscale modeling of the sintering process of printed nanoinks, Comput. Math. Appl. 78 (7) (2019) 2325–2337, https://doi.org/10.1016/j.camwa.2018.07.024, Simulation for Additive Manufacturing.

[17] J. Dantzig, Modelling liquid-solid phase changes with melt convection, Int. J. Numer. Methods Eng. 28 (8) (1989) 1769–1785.

[18] J. Dantzig, M. Rappaz, Solidification, EPFL Press, 2016.

[19] A. Özcan, S. Kollmannsberger, J. Jomo, E. Rank, Numerical simulation of selective laser melting processes with multi-level hp-adaptive finite cell method, in: 10th International Conference on Advanced Computational Engineering and Experimenting, 2016.

[20] B. Peters, X. Besseron, A. Estupinan, A. Mahmoudi, M. Mohseni, A discrete/continuous numerical approach to multi-physics, IFAC-PapersOnLine 48 (1) (2015) 645–650, https://doi.org/10.1016/j.ifacol.2015.05.141.

[21] Y. Zhang, G. Guillemot, M. Bernacki, M. Bellet, Macroscopic thermal finite element modeling of additive metal manufacturing by selective laser melting process, Comput. Methods Appl. Mech. Eng. 331 (2018) 514–535, https://doi.org/10.1016/j.cma.2017.12.003.

[22] Y. Zhang, Q. Chen, G. Guillemot, C.-A. Gandin, M. Bellet, Numerical modelling of fluid and solid thermomechanics in additive manufacturing by powder-bed fusion: continuum and level set formulation applied to track- and part-scale simulations, C. R., Méc. 346 (11) (2018) 1055–1071, https://doi.org/10.1016/j.crme.2018.08.008.

[23] T. Shao, M. Hua, H. Tam, E.H. Cheung, An approach to modelling of laser polishing of metals, Surf. Coat. Technol. 197 (1) (2005) 77–84, https://doi.org/10.1016/j.surfcoat.2005.01.010.

[24] A. Bonito, A. Caboussat, M. Picasso, J. Rappaz, A numerical method for fluid flows with complex free surfaces, in: R. Glowinski, P. Neittaanmäki (Eds.), Partial Differential Equations, in: Computational Methods in Applied Sciences, vol. 16, Springer Netherlands, 2008, pp. 187–208.

[25] A. Caboussat, A numerical method for the simulation of free surface flows with surface tension, Comput. Fluids 35 (10) (2006) 1205–1216.

[26] A. Caboussat, P. Clausen, J. Rappaz, Numerical simulation of two-phase flow with interface tracking by adaptive Eulerian grid subdivision, Math. Comput. Model. 55 (2012) 490–504.

[27] A. Caboussat, M. Picasso, J. Rappaz, Numerical simulation of free surface incompressible liquid flows surrounded by compressible gas, J. Comput. Phys. 203 (2) (2005) 626–649.

[28] A. Bonito, M. Picasso, M. Laso, Numerical simulation of 3D viscoelastic flows with free surfaces, J. Comput. Phys. 215 (2) (2006) 691–716.

[29] G. Jouvet, M. Huss, H. Blatter, M. Picasso, J. Rappaz, Numerical simulation of Rhonegletscher from 1874 to 2100, J. Comput. Phys. 228 (17) (2009) 6426–6439.

[30] M. Rappaz, M. Bellet, M. Deville, Modeling in Materials Science and Engineering, Springer Series in Computational Mathematics, Springer Verlag, Berlin Heidelberg, 2003.

[31] G.P. Sasmal, J.I. Hochstein, Marangoni convection with a curved and deforming free surface in a cavity, J. Fluids Eng. 116 (3) (1994) 577–582.

[32] Z.S. Saldi, Marangoni driven free surface flows in liquid weld pools, Ph.D. thesis, Department of MultiScale Physics, Faculty of Applied Sciences, Delft University of Technology, Delft, The Netherlands, 2012.

[33] P. Sun, C. Liu, J. Xu, Phase field model of thermo-induced Marangoni effects in the mixtures and its numerical simulations with mixed finite element method, Commun. Comput. Phys. 6 (2009) 1095–1117.

[34] G.I. Marchuk, Splitting and alternating direction methods, in: Handbook of Numerical Analysis, Vol. I, North-Holland, Amsterdam, 1990, pp. 197–462.

[35] W.F. Noh, P. Woodward, SLIC (simple line interface calculation), in: Proceedings of the Fifth International Conference on Numerical Methods in Fluid Dynamics, vol. 59, 1976, pp. 330–340.

[36] V. Maronnier, M. Picasso, J. Rappaz, Numerical simulation of three dimensional free surface flows, Int. J. Numer. Methods Fluids 42 (7) (2003) 697–716.

[37] A. Großmann, J. Felger, T. Froelich, J. Gosmann, C. Mittelstedt, Melt pool controlled laser powder bed fusion for customised low-density lattice structures, Mater. Des. 181 (2019) 108054, https://doi.org/10.1016/j.matdes.2019.108054.

[38] S. Boyaval, A. Caboussat, A. Mrad, M. Picasso, G. Steiner, A semi-Lagrangian splitting method for the numerical simulation of sediment transport with free surface flows, Comput. Fluids 172 (2018) 384–396, https://doi.org/10.1016/j.compfluid.2018.04.002.

[39] M. Ishii, N. Zuber, Drag coefficient and relative velocity in bubbly, droplet or particulate flows, AIChE J. 25 (5) (1979) 843–855, https://doi.org/10.1002/aic.690250513.

[40] F. Verhaeghe, T. Craeghs, J. Heulens, L. Pandelaers, A pragmatic model for selective laser melting with evaporation, Acta Mater. 57 (20) (2009) 6006–6012, https://doi.org/10.1016/j.actamat.2009.08.027.

[41] M.M. Francois, J.M. Sicilian, D. Kothe, Modeling of thermocapillary forces within a volume tracking algorithm, in: Modeling of Casting, Welding and Advanced Solidification Processes – XI 2, 2006, pp. 935–942.

[42] A. Berger, H. Brezis, J. Rogers, A numerical method for solving the problem $u_t - \delta f(u) = 0$, RAIRO Numer. Anal. 13 (4) (1979) 297–312.

[43] E. Magenes, R.H. Nochetto, C. Verdi, Energy error estimates for a linear scheme to approximate nonlinear parabolic problems, ESAIM: M2AN 21 (4) (1987) 655–678, https://doi.org/10.1051/m2an/1987210406551.

[44] Y. Safa, M. Flueck, J. Rappaz, Numerical simulation of thermal problems coupled with magnetohydrodynamic effects in aluminium cell, Appl. Math. Model. 33 (3) (2009) 1479–1492, https://doi.org/10.1016/j.apm.2008.02.011.

[45] R. Pardeshi, V. Voller, A. Singh, P. Dutta, An explicit–implicit time stepping scheme for solidification models, Int. J. Heat Mass Transf. 51 (13) (2008) 3399–3409, https://doi.org/10.1016/j.ijheatmasstransfer.2007.11.060.

[46] M. Paolini, G. Sacchi, C. Verdi, Finite element approximations of singular parabolic problems, Int. J. Numer. Methods Eng. 26 (9) (1988) 1989–2007.

[47] J.-F. Gerbeau, T. Lelièvre, C. Le Bris, Simulations of MHD flows with moving interfaces, J. Comput. Phys. 184 (1) (2003) 163–191, https://doi.org/10.1016/S0021-9991(02)00025-6.

[48] R. Franke, Scattered data interpolation: test of some methods, Math. Comput. 38 (1982) 181–200, https://doi.org/10.2307/2007474.

[49] COMSOL, Tin melting front, comsol multiphysics v 5.6, https://www.comsol.com/model/tin-melting-front-6234. (Accessed 20 February 2023).

[50] W. Pitscheneder, T. Debroy, K. Mundra, R. Ebner, Role of sulfur and processing variables on the temporal evolution of weld pool geometry during multikilowatt laser beam welding of steels, Weld. Res. 75 (1996) 71–80.

[51] P. Sahoo, T. Debroy, M.J. McNallan, Surface tension of binary metal – surface active solute systems under conditions relevant to welding metallurgy, Metall. Trans. B 19 (3) (1988) 483–491, https://doi.org/10.1007/BF02657748.